



Wind Direction Retrieval Using Spaceborne GNSS-R in Nonspecular Geometry

Guodong Zhang , Dongkai Yang, Yongqing Yu, and Feng Wang 

Abstract—A wind direction retrieval algorithm using spaceborne global navigation satellite system reflectometry (GNSS-R) in nonspecular geometry is presented. This article first focuses on investigating the influence of wind direction on the scattering strength purely in specular geometry and nonspecular geometry. The sensitivity of the scattered GNSS signals in nonspecular geometry to wind direction is demonstrated despite the weaker power level. Therefore, a wind direction retrieval algorithm based on the geophysical model function (GMF) whose parameters are parameterized as a look-up-table is proposed. Then, the spatial resolution and power link of the spaceborne GNSS-R in nonspecular geometry are analyzed. The incidence angle of the scattered signals ranges 15° to 35° to ensure the sensitivity to wind direction and the power level of scattered signals. The retrieving results using simulated data show that the ambiguity of the measurement geometry can be eliminated by using the multisatellite observation, and two possible wind directions for the same corresponding observable are obtained in the wind direction retrieval algorithm. The accuracy of wind speed importantly impacts on the retrieving performance of wind direction, therefore, it is needed to improve the measuring accuracy of wind speed. These results provide information to guide the wind direction retrieval using spaceborne GNSS-R in nonspecular geometry.

Index Terms—Global navigation satellite system reflectometry (GNSS-R), nonspecular geometry, wind direction.

I. INTRODUCTION

GLOBAL navigation satellite system reflectometry (GNSS-R) that was primarily proposed for ocean mesoscale altimetry by Martin-Neira [1] has been significantly extended to a wide range of applications as an emerging earth remote sensing technology. GNSS-R uses the global navigation satellite signals that are reflected off the Earth's surface, to retrieve various earth physical parameters such as ocean surface altimetry [2]–[4], wind speed [5], sea ice [6], [7], significant wave height [8], soil moisture [9], target detection [10], [11], etc. The potential for global observation

Manuscript received September 29, 2019; revised December 12, 2019; accepted December 30, 2019. Date of publication February 6, 2020; date of current version February 20, 2020. This work was supported in part by the National Key Research and Development Plan under Grant 2017YFB0502802 and in part by the National Natural Science Foundation of China under Grant 41774028. (Corresponding author: Dongkai Yang.)

Guodong Zhang, Dongkai Yang, and Feng Wang are with the School of Electronic and Information Engineering, Beihang University, Beijing 100083, China (e-mail: guodongzhang_q@163.com; yangdongkai@sina.com; wangf.19@163.com).

Yongqing Yu is with the Shengli Oil Field of China Petroleum and Chemical Corporation, Haiyang Oil Production Plant, Dongying 257000, China (e-mail: 314589040@qq.com).

Digital Object Identifier 10.1109/JSTARS.2020.2970106

of geophysical parameters using GNSS-R has been greatly exploited with the implementation of spaceborne GNSS-R missions, including UK-DMC [12], UK-TDS-1 [13], and Cyclone Global Navigation Satellite System (CYGNSS) [14].

Ocean wind speed and direction have continuously been the major areas of attention within the essential climate variables. At present, ocean wind vector, especially wind direction, is primarily measured by the scatterometer, an active microwave instrument, which relies solely on oblique angle backscatter. Moreover, the retrieval of ocean wind speed using GNSS-R has already been extensively discussed all over the world and made significant progress, especially in global observations [15]–[17]. However, a few studies focused on determining the wind direction. Wind direction was found to correspond to the anisotropy in probability density function (PDF) of ocean surface slope, which can be estimated from the airborne reflected GPS waveforms [18]. The influence of wind vector on the trailing edge of the airborne reflected GPS waveforms was explored in [19], where the impact of the basic contributing features were analyzed one by one. Wind direction was obtained using a multisatellite nonlinear least squares approach based on the delay waveform of airborne GNSS-R, which corresponded with QuikSCAT measurements at the 30° level [20]. The skewness angle was designated to measure the delay-Doppler map (DDM) asymmetry metrics and modeled as a function of wind direction, which was validated in an airborne experiment [21]. For spaceborne GNSS-R, the low sensitivity of the normalized peak SNR to the wind direction was observed through investigating the GNSS-R measurements collected by UK-TDS-1 [22]. The possibility of wind direction observation using spaceborne GNSS-R observables was investigated theoretically, and two metrics of DDM were proposed to retrieve wind direction from the DDM asymmetry, which were explored using the simulation tool P2EPS [23].

The abovementioned research works on wind direction retrieval mainly focused on the signals reflected off the surface in the general specular geometric observation configuration. The sensitivity of the bistatic radar cross section to wind direction was assessed using the model with small slope approximation, a more accurate approximation in [24], and the research has shown that GNSS scattered signals only away from the nominal specular direction can be used to retrieve wind direction. Similarly, Park and Johnson found that the wind direction dependencies of the near-specular DDM-average (DDMA) were negligible, and proposed that wind direction in spaceborne GNSS-R should be retrieved only from the DDM

away from the specular region [25]. A wind direction retrieval algorithm using low-altitude GNSS-R in backward geometry was proposed and examined using the simulated data [26]. The disadvantage of the method using backward scattered GNSS signals is low-power level of the received signals, particularly for spaceborne GNSS-R, although it has been confirmed that backward scattered GNSS signals could be received from the airborne platform in [26]. Therefore, the sensitivity to wind direction and the power level of scattered signals should be compromised to select the appropriate scattering geometry of the observation, when attempting to retrieve wind direction using GNSS-R. Based on the previous description and the published research works mentioned above, it is more likely to retrieve wind direction from spaceborne GNSS-R observables using the slightly nonspecular observation geometry between the purely specular and backward.

In this article, the feasibility of retrieving wind direction from the spaceborne GNSS-R observables in nonspecular geometry is explored, and the retrieving performance is assessed by the theoretical simulation. The rest of this article is organized as follows. Section II reviews the DDM theoretical model. Section III presents the wind direction retrieval algorithm including the retrieval geometry, the scattering of sea surface, and the algorithm steps in detail. Section IV illustrates the application of the retrieval algorithm to a simulated dataset, describing the simulation, investigating the spatial resolution and the power link, and summarizing the derivation of the geophysical model function (GMF). Section V contains an analysis of the retrieval algorithm performances using the simulated dataset. Finally, Section VI concludes this article.

II. SCATTERING MODEL OF GNSS-R

The theoretical scattering model for the DDM that represents the distribution of the correlation power in delay-Doppler domain is first derived by Zavorotny and Voronovich, which is based on the geometric optics limit of Kirchhoff approximation. The model is expressed as [27]

$$P(\tau, f) = \frac{T_{\text{coh}}^2 P_t G_t \lambda^2}{(4\pi)^3} \times \int \frac{G_r(\rho) \Lambda^2(\tau - \tau(\rho)) S^2(T_{\text{coh}}(f - f(\rho)))}{R_t^2(\rho) R_r^2(\rho)} \sigma^2(\rho) d\rho \quad (1)$$

where T_{coh} is the coherent integration time; P and P_t are the received and transmitted signal power; G_r and G_t are the receiving and transmitting antenna gain; R_t and R_r are the ranges of GNSS satellite to coordinate origin and coordinate origin to receiver; λ is the electromagnetic wavelength of the signal; $\Lambda(\cdot)$ is the PRN code autocorrelation function defined as $\Lambda(\tau) = 1 - |\tau|/\tau_c$, with τ_c being the length of the PRN code chip; $S(\cdot)$ is the sinc-shaped function defined as $S(f) = \sin(\pi f)/\pi f$; σ is the bistatic radar cross section (BRCS); and ρ is the arbitrary surface point.

The DDM, $P(\tau, f)$, corresponds to the power of the scattered GNSS signal as a function of the time delay τ and Doppler frequency shift f . And it is jointly determined by several parameters such as the receiving antenna gain, the propagation path, and the BRCS. However, when the configuration of GNSS satellite

and the spaceborne receiver is known, the parameters other than the BRCS are also known. In the case of the same observation configuration, the distribution of DDM is entirely determined by the ocean surface scattering that is largely affected by the wind speed and direction.

A. Geometry

GNSS-R operates in a noncooperative and bistatic radar configuration with GNSS satellites as transmitters and receivers located on other platforms (including ground, aircraft, and low earth orbit satellite). There are forward and backward observation geometries in GNSS-R, and the forward observation geometry includes purely specular and nonspecular geometries. For a purely specular geometry, the specular reflection point on the Earth surface, the observation center, can be determined based on the GNSS-R receiver and transmitter locations. At this point, the incident polar angle from the transmitter is equal to the scattered polar angle to the receiver. However, for a nonspecular geometry in this article, the observation center is located in the main beam of the receiver nadir antenna footprint. For the spaceborne forward GNSS-R, the general purely specular and nonspecular geometries corresponding to one reflecting surface point are illustrated in Fig. 1, where the local coordinate systems are defined as follows.

- 1) One of the two coordinate origins is on the specular reflection point in Fig. 1(a), and the other is on the pointing location of the left-hand circularly polarization (LHCP) antenna beam center on the Earth surface in Fig. 1(b).
- 2) The Z-axis coincides with the normal vector of the Earth surface and is positive outward.
- 3) The GNSS and LEO satellites are located on the Y-Z coordinate plane, and their Z-axis coordinates are positive.
- 4) The X-axis completes the Cartesian coordinate system.
- 5) The wind direction of this article is defined as the angle between the wind vector and the incident plane.

Fig. 1(a) illustrates the general purely specular geometry. Fig. 1(b) illustrates the nonspecular geometry. Both of them are single satellite scattering, and the heights of GNSS and LEO satellites are 20200 km and 510 km, respectively. In particular, this article adopts the subsatellite observation configuration in the nonspecular geometry because of simplicity and achievability. Spaceborne receivers in the nonspecular geometry would receive signals scattered from areas far from the specular reflection point. The distance between the specular reflection point and the nonspecular observation center, for example, with a 20° incidence angle, would be about 159 km.

The signal is incident from the GNSS satellite at the polar angle θ_i and the azimuthal angle φ_i , and then scattered to the LEO satellite at the polar angle θ_s and the azimuthal angle φ_s . According to the polar angle and the azimuthal angle, the ranges of GNSS satellite to coordinate origin and coordinate origin to LEO satellite are respectively [22]

$$R_t = \sqrt{(H_t + R_e)^2 - R_e^2 \sin^2 \theta_i} - R_e \cos \theta_i \quad (2)$$

$$R_r = \sqrt{(H_r + R_e)^2 - R_e^2 \sin^2 \theta_s} - R_e \cos \theta_s \quad (3)$$

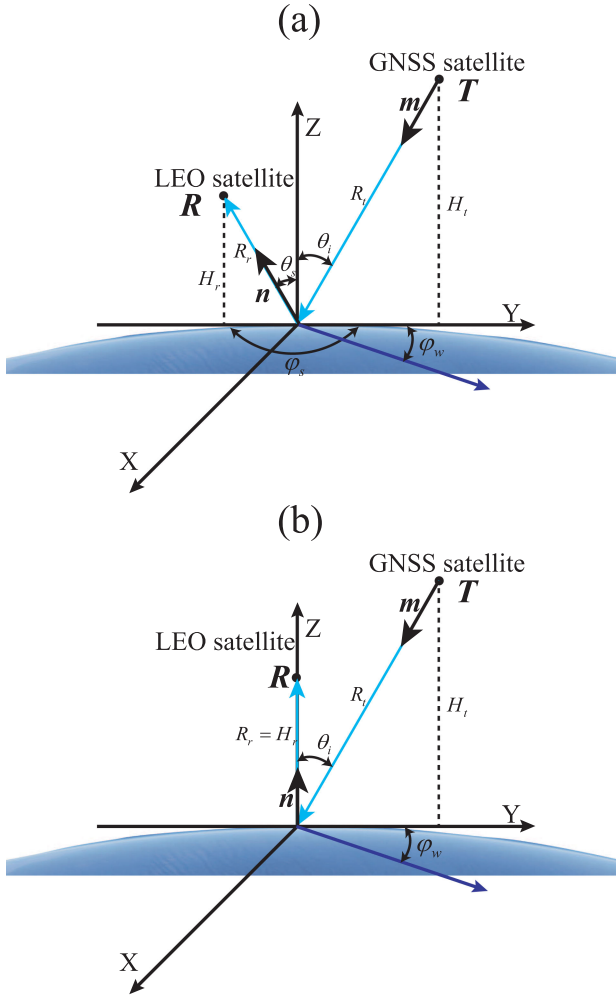


Fig. 1. Bistatic geometries of (a) purely specular observation and (b) nonspecular observation for the spaceborne forward GNSS-R.

where H_t and H_r are the heights of GNSS and LEO satellite, respectively; R_e is the earth radius.

The definition of the scattering vector \mathbf{q} is as follows:

$$\mathbf{q} = \mathbf{n} - \mathbf{m} = \hat{\mathbf{x}}q_x + \hat{\mathbf{y}}q_y + \hat{\mathbf{z}}q_z \quad (4)$$

where $\hat{\mathbf{x}}$, $\hat{\mathbf{y}}$, and $\hat{\mathbf{z}}$ are the unit vectors of the X -axis, Y -axis, and Z -axis, respectively; \mathbf{m} and \mathbf{n} are the corresponding incident and scattered unit wave vectors and defined as

$$\mathbf{m} = \hat{\mathbf{x}} \sin \theta_i \sin \varphi_i + \hat{\mathbf{y}} \sin \theta_i \cos \varphi_i - \hat{\mathbf{z}} \cos \theta_i \quad (5)$$

$$\mathbf{n} = \hat{\mathbf{x}} \sin \theta_s \sin \varphi_s + \hat{\mathbf{y}} \sin \theta_s \cos \varphi_s + \hat{\mathbf{z}} \cos \theta_s. \quad (6)$$

From the definition mentioned above, $\theta_i = \theta_s$, $\varphi_i = 0^\circ$, and $\varphi_s = 180^\circ$ for a purely specular geometry illustrated in Fig. 1(a). θ_i is in the range of $[0^\circ, 90^\circ]$, $\theta_s = 0^\circ$ and $\varphi_i = 0^\circ$ for a nonspecular geometry illustrated in Fig. 1(b).

B. Scattering of Sea Surface

When incident on the sea surface, electromagnetic wave will interact with the sea surface and be scattered (including specular and diffuse scattering). The scattering of different rough sea

surface is quite different. As the sea surface becomes rough, specular scattering tends to decrease while diffuse scattering tends to increase. It has been repeatedly demonstrated that the scattering of GNSS signals on the sea surface is primarily diffuse scattering. In other words, the GNSS signals scattered from the sea surface are mostly incoherent. The BRCS has been defined as the ratio of scattered signal power and incident signal power to describe the rough surface scattering. Several scattering models have been proposed to theoretically calculate the BRCS of the sea surface. And the most practical tool among them until now has been the two-scale surface model, which is based on the theory that the sea surface is the superposition of two-scale roughness surface.

In the two-scale surface model, the large-scale and small-scale roughness of the sea surface are modeled as two independent random processes. Therefore, BRCS of sea surface is computed by the sum of large-scale and small-scale BRCS, which could be estimated using the Kirchhoff approximation in the geometric optics (KAGO) and small perturbation method (SPM), respectively [22],

$$\sigma = \sigma_{\text{KAGO}} + \sigma_{\text{SPM}} \quad (7)$$

where σ_{KAGO} and σ_{SPM} are BRCS of the large-scale and small-scale roughness, respectively. σ_{KAGO} is computed as [27]

$$\sigma_{\text{KAGO}} = \pi |\Re|^2 \frac{|\mathbf{q}_\perp|^4}{q_z^4} P_{\text{pdf}} \left(-\frac{\mathbf{q}_\perp}{q_z} \right) \quad (8)$$

where \Re is the Fresnel coefficient, \mathbf{q}_\perp and q_z stand for the horizontal and vertical components of the scattering vector $\mathbf{q} \equiv (\mathbf{q}_\perp, q_z)$; $P_{\text{pdf}}(\mathbf{s})$ is the PDF of the mean square slope of sea surface, which here is assumed as 2-D anisotropic Gaussian distribution and described as

$$P_{\text{pdf}}(\mathbf{s}) = \frac{1}{2\pi \sqrt{\det(\mathbf{M})}} \exp \left[-\frac{1}{2} \mathbf{s}^T \mathbf{M}^{-1} \mathbf{s} \right] \quad (9)$$

where \mathbf{M} is the matrix of slope second order moments:

$$\mathbf{M} = \begin{bmatrix} \cos \varphi_w & -\sin \varphi_w \\ \sin \varphi_w & \cos \varphi_w \end{bmatrix} \begin{bmatrix} \sigma_u^2 & 0 \\ 0 & \sigma_c^2 \end{bmatrix} \times \begin{bmatrix} \cos \varphi_w & \sin \varphi_w \\ -\sin \varphi_w & \cos \varphi_w \end{bmatrix} \quad (10)$$

where φ_w is the wind direction, σ_u^2 and σ_c^2 are the mean-square slopes along the up-wind and cross-wind axes. For small-scale roughness, the BRCS, σ_{SPM} , is computed as [28]

$$\sigma_{\text{SPM}} = 8 |k^2 \cos \theta_i \cos \theta_s \Re|^2 S(2k \sin \theta_i, \varphi_{i,w}, U_{10}) \quad (11)$$

where k is the wave number of the incident signal; $S(2k \sin \theta_i, \varphi_{i,w}, U_{10})$ is the unified directional spectrum of ocean surface, which can be obtained by using Elfouhaily spectrum [29]; $\varphi_{i,w}$ is the azimuthal angle of the incident signal relative to the wind vector; U_{10} is the wind speed at 10 m above the ocean surface.

III. WIND DIRECTION RETRIEVAL ALGORITHM

The sensitivity of the BRCS to wind vector for spaceborne GNSS-R in purely specular and nonspecular geometry is shown

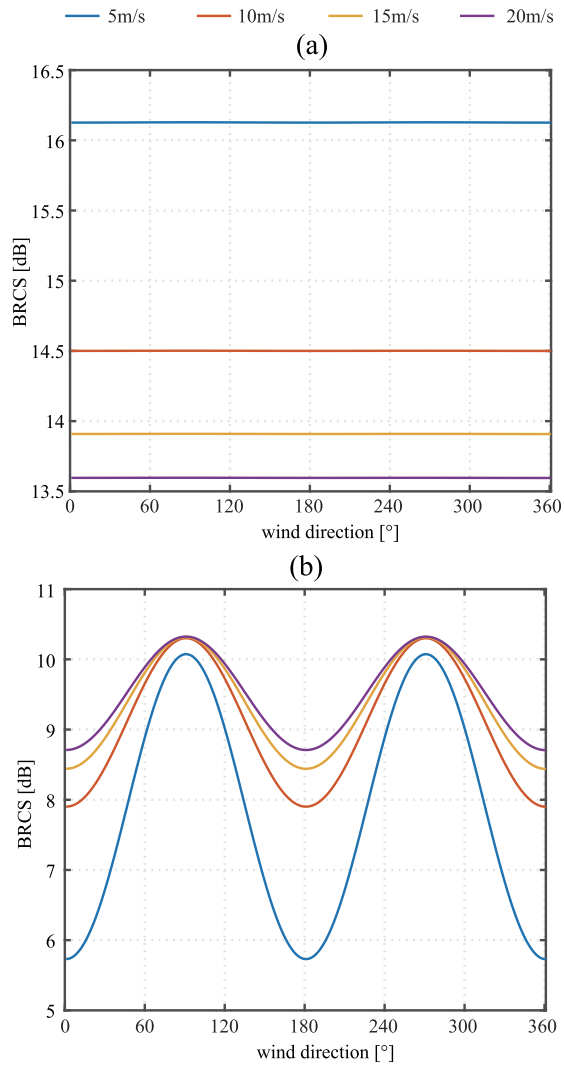


Fig. 2. Curves of the BRCS versus the wind direction for different wind speeds, illustrated for spaceborne GNSS-R in (a) purely specular and (b) nonspecular geometry. The BRCS for both case are computed using the two-scale surface model at 20° incidence.

in Fig. 2, which is computed using the two-scale surface model at 20° incidence. It can be seen that the BRCS of the purely specular geometry is heavily affected by wind the speed rather than wind direction. And the variation of BRCS over wind direction is typically small and unlikely to be useful in practice for sensing wind direction using only a purely specular geometry, which is similar to the conclusion drawn in [25]. However, the BRCS of the nonpurely specular geometry is not only determined by wind speed, but also by wind direction. Therefore, it is possible to retrieve wind direction using spaceborne GNSS-R in the nonpurely specular geometry.

It is worth noting that the BRCS of the nonpurely specular geometry increases as the wind speed increases, which is contrary to the purely specular geometry. And it is lower than the purely specular scattering, which means that it is more difficult for the spaceborne receiver to receive and process the scattered signal in the nonspecular geometry. Furthermore, from the plots

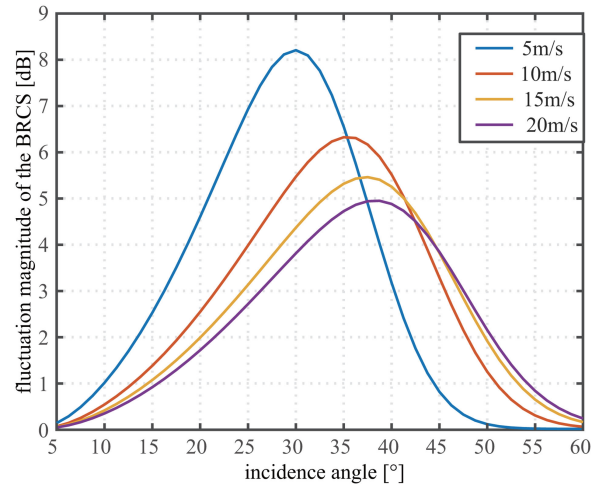


Fig. 3. Curves of the fluctuation magnitude of BRCS with wind direction versus the incidence angle for different wind speeds, illustrated for spaceborne GNSS-R in nonpurely specular geometry.

in Fig. 2(b), it can be concluded that wind direction will present four possible solutions if it is retrieved from a single GNSS-R measurement.

Fig. 3 shows the fluctuation magnitude of the BRCS with wind direction for spaceborne GNSS-R in nonspecular geometry of different incidence angles. It is clear from Fig. 3 that the fluctuation magnitude of BRCS with wind direction increases first and then decreases as the incidence angle increases. This suggests that wind direction observation may be more accurate for the spaceborne GNSS-R in nonspecular geometry when the incidence angles range between 15° and 50° . Additionally, it is more difficult for the spaceborne receiver to receive and process the scattered signal of the nonspecular geometry if the incidence angle is larger. Therefore, the fluctuation amplitude and strength of BRCS should be considered simultaneously to select the appropriate incidence angle.

As mentioned above, the BRCS of the nonpurely specular geometry appears obvious periodic fluctuation with wind direction. Therefore, the retrieval algorithm presented here also use the DDM observable, the DDMA, which is analogous to the wind speed retrieval algorithm explained in [15]. The DDMA is the average of the BRCS over a given delay-Doppler range window around the pointing location of the LHCP antenna beam center, which is calculated from the DDM after removal of the additive noise floor as explained in [30]. The delay and Doppler range of the retrieval algorithm should be chosen appropriately to meet the baseline spatial resolution requirement of 25×5 km.

The wind direction retrieval algorithm is performed in two steps. First, the near-specular DDM measured by the receiving antenna on the front or rear side of the subsatellite track is used to retrieve wind speed by a best weighted estimator, which has been explained in [15]. Second, the nonspecular DDM measured by the receiving antenna on the below side of the subsatellite track is used to retrieve wind direction. Specifically, wind direction is estimated from the DDMA derived from nonspecular DDM using GMF, after obtaining the wind speed corresponding to the same observation area.

TABLE I
 PARAMETERS USED TO COMPUTE THE SNR

Symbol	Parameter	Value
P_t	Transmitted signal power	26.8 W
G_t	Transmitting antenna gain	12.1 dB
H_t	Transmitter altitude	20200 km
H_r	Receiver altitude	510 km
G_r	Receiving antenna gain	12.1 dB
T_{coh}	Coherent integration time	1 ms
N_{incoh}	Number of incoherent averaging	1000
D_c	Ideal detection factor	26.3
k_B	Boltzmann's constant	1.38×10^{-23} km
B	Receiver bandwidth	2.5 MHz
T_K	Receiver temperature	25°C
θ_i	Incidence angle	[0, 90°]
φ_w	Wind direction	90°

IV. WIND DIRECTION RETRIEVAL FROM SIMULATED DATA

A. Simulation Studies

In the framework of the development of a generic GNSS-R space mission, the end-to-end performance simulator is usually developed to analyze the spaceborne and instrument in an efficient and convenient manner. There are already several simulators such as the CYGNSS end-to-end simulator [31] and the PAU/PARIS end-to-end performance simulator (P2EPS) [32]. Moreover, the real spaceborne datasets from TDS-1 and CYGNSS are in the traditional specular geometry rather than the nonspecular geometry proposed in this article, which cannot be used to verify the proposed method. Therefore, a simulator has been developed to better analyze the feasibility of retrieving wind direction using the spaceborne GNSS-R observables in nonspecular geometry illustrated in Fig. 1(b). The parameters of the simulator are shown in Table I, which are used to compute the BRCSs of different wind speeds and directions and then generate corresponding DDMs. In addition, the incidence angle of the simulator ranges 15° to 35° to ensure the sensitivity to wind direction and the power level of scattered signals.

In practical applications, due to the presence of noise during the reception and processing of the scattered GNSS signal, the DDM after coherent integration contains the multiplicative speckle and additive thermal noise. The multiplicative speckle noise is usually assumed to be a unit-mean exponential distribution [33], which can be reduced by the incoherent averaging. The power of the additive thermal noise can be expressed as a function of coherent integration time [34].

As an example, Fig. 4 provides a simulated DDM after 1 ms coherent integration and 1000 incoherent averaging for the spaceborne GNSS-R in nonpurely specular geometry. It is worth to note that the DDM of nonpurely specular geometry is similar to the tail of the typical ‘‘horseshoe shape,’’ which is primarily caused by the scattering region away from the specular reflection point.

B. Power Link

As mentioned above, the BRCS of the nonpurely specular geometry is lower than the purely specular scattering. In order

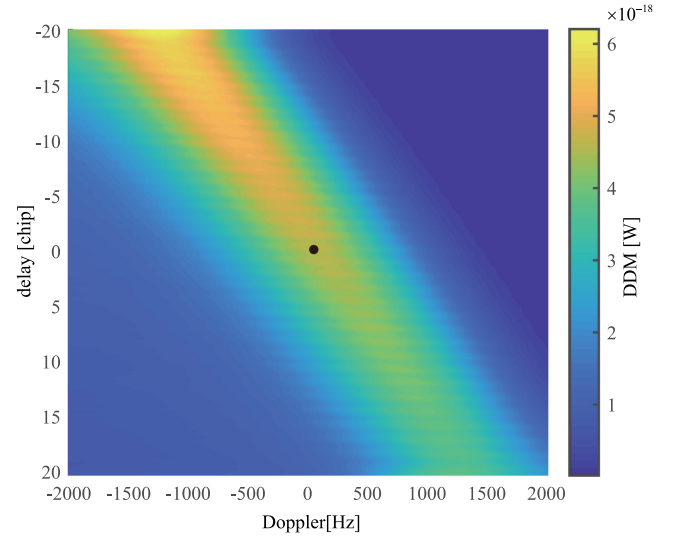


Fig. 4. Simulated DDM of spaceborne GNSS-R in nonspecular geometry for the wind speed of 15 m/s, the wind direction of 90°, the incidence angle of 20°. The black dot is the time delay-Doppler position of the scattered GNSS signals from LHCP antenna beam center, and its coordinate value is [0 Hz, 0 chip].

to investigate the possibility to retrieve wind direction using the spaceborne GNSS-R in nonspecular geometry, the power link of the scattered GNSS signal in the nonspecular geometry is evaluated by the radar equation. For the bistatic observation, the radar equation can be expressed as [35]

$$P_r = \frac{P_t G_t \lambda^2 G_r \sigma A}{(4\pi)^3 R_t^2 R_r^2} \quad (12)$$

where P_r is the received signal power, A is the size of the observation area, which is generally computed as the area surrounded by the specific iso-delay and iso-Doppler lines for the spaceborne GNSS-R.

The scattered GNSS signal is coherently integrated and incoherently averaged to improve the signal-to-noise ratio (SNR). The final SNR can be expressed as follows:

$$\text{SNR} = 10 \lg \left(\frac{P_r}{P_{\text{noise}}} \right) + G_{\text{coh}}(T_{\text{coh}}) + G_{\text{incoh}}(N_{\text{incoh}}) \quad (13)$$

where P_{noise} is the noise power; G_{coh} and G_{incoh} are the gain of coherent integration and incoherent averaging, respectively; N_{incoh} is the number of incoherent averaging. G_{coh} is computed as

$$G_{\text{coh}}(T_{\text{coh}}) = 10 \lg \left(\frac{T_{\text{coh}}}{T_{\text{chip}}} \right) \quad (14)$$

where T_{chip} is the chip width and G_{incoh} is computed as [36]

$$G_{\text{incoh}}(N_{\text{incoh}}) = 10 \lg(N_{\text{incoh}}) - 10 \lg \left(\frac{1 + \sqrt{1 + 9.2 N_{\text{incoh}} / D_c}}{1 + \sqrt{1 + 9.2 / D_c}} \right) \quad (15)$$

where D_c is the ideal detection factor. It is 26.3 when the detection and false alarm probability are 98% and 10^{-7} , respectively.

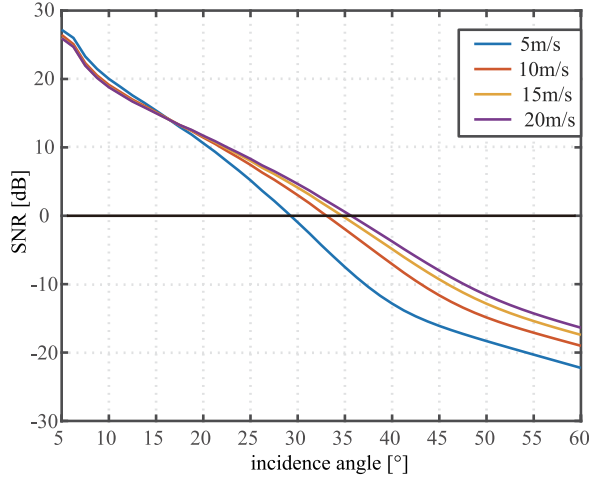


Fig. 5. Curves of the SNR versus the incidence angle for different wind speeds, illustrated for spaceborne GNSS-R in nonpurely specular geometry.

There are speckle and thermal noises in the scattered GNSS signal. The speckle noise level can be reduced by the incoherent accumulations of consecutive cross-correlation values. Therefore, for the sake of analysis, it is assumed that there is only thermal noise. P_{noise} can be computed as

$$P_{\text{noise}} = k_B B T_K \quad (16)$$

where k_B is the Boltzmann's constant; B is the receiver bandwidth; T_K is the receiver temperature.

In order to compute (13), the parameters used are listed in Table I, where values are reported assuming GPS as the transmitting GNSS and CYGNSS as the receiving platform. The behavior of the SNR as a function of the incidence angle for spaceborne GNSS-R in nonspecular geometry is shown in Fig. 5. The SNR can be seen to monotonically decrease as the incidence angle increases, as expected. Because the observation area is further away from the specular region as the incidence angle increases, which means the power level of the scattered GNSS signal is lower.

In order to reduce the power uncertainty of the nonspecular GNSS-R reflections, we only consider the DDM with the SNR higher than 0 dB. In fact, this assumption is well justified due to the fact that the standard deviation of the power observation is only increased by a factor of 2 with an SNR of 0 dB comparing to the thermal noise free case [37], [38]. In the case of parameters listed in Table I, the incidence angle should be limited less than 35° . However, if the receiving antenna gain is higher, the available range of incidence angle will be larger. Therefore, it is necessary to develop the high-gain receiving antenna and high-sensitivity receiver to improve the SNR for the spaceborne receiver in the nonspecular geometry.

C. Delay and Doppler Range Selection

As a crucial indicator of remote sensing application, the spatial resolution should be appropriately determined according to different application requirements. In the case of coastal or airborne GNSS-R, the spatial resolution is generally considered

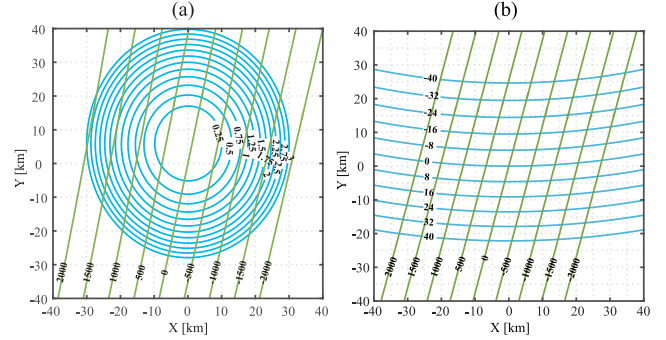


Fig. 6. Isodelay lines (blue, in chips) and iso-Doppler lines (green, in Hz), illustrated for (a) a purely specular geometry and (b) a nonpurely specular geometry where the angle between the LEO satellite velocity and the incident plane is 75° .

to be the coverage area of the receiver antenna. However, in the case of spaceborne GNSS-R, the coverage area and the glistening zone are usually in the 100-km range, including multiple lines of constant delay (iso-delay) and constant Doppler frequency shift (iso-Doppler). The time delay and the Doppler frequency shift for the signal scattering off the arbitrary surface point $\mathbf{S}_{x,y}$ relative to the coordinate origin \mathbf{S}_o are respectively

$$\tau_{x,y} = \frac{|\mathbf{T} - \mathbf{S}_{x,y}| + |\mathbf{R} - \mathbf{S}_{x,y}|}{c} - \frac{|\mathbf{T} - \mathbf{S}_o| + |\mathbf{R} - \mathbf{S}_o|}{c} \quad (17)$$

$$f_{x,y} = \frac{\mathbf{v}_t \cdot \mathbf{m}_{x,y} - \mathbf{v}_r \cdot \mathbf{n}_{x,y}}{\lambda} - \frac{\mathbf{v}_t \cdot \mathbf{m}_o - \mathbf{v}_r \cdot \mathbf{n}_o}{\lambda} \quad (18)$$

where \mathbf{T} and \mathbf{R} are the locations of GNSS and LEO satellite; c is the speed of light; \mathbf{v}_t and \mathbf{v}_r are the velocities of GNSS and LEO satellite. Therefore, different scattering units have different time delays and the Doppler frequency shifts. There is a correspondence between points on the delay-Doppler plane and points on the sea surface plane, but not the one-to-one correspondence.

Fig. 6 shows the iso-delay and iso-Doppler lines of the purely specular and nonspecular geometry as illustrated in Fig. 1 for the equal incidence angle θ_i and azimuth angle φ_i . The isodelay lines of the purely specular geometry are getting closer to each other as the delay increases. Therefore, the difference between the iso-delay lines of the nonspecular geometry is greater in the case of the same spatial distance. Furthermore, the area of the spatial footprint corresponding to the same delay and Doppler range in the nonspecular geometry is related to the angle between the isodoppler lines and the isodelay lines as shown in Fig. 6(b). The angle is mainly affected by the angle between the LEO satellite velocity and the incident plane because of the low GNSS velocity. Therefore, as an example, the angle between the LEO satellite velocity and the incident plane is 75° in the nonspecular geometric analysis of this section.

The spatial resolution in this article is the square root of the instantaneous field of view, which was as defined in [15]. Therefore, the spatial resolution of the spaceborne GNSS-R is determined by the delay and Doppler range, over which the observables are computed. Fig. 7 shows curves of the spatial resolution versus the incidence angle for different delay ranges

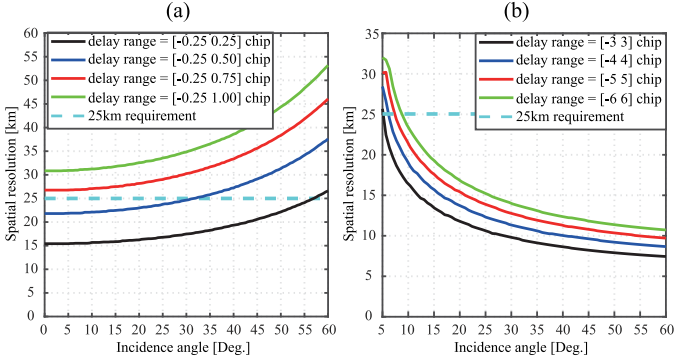


Fig. 7. Curves of the spatial resolution versus the incidence angle for different delay ranges, illustrated for spaceborne GNSS-R in (a) a purely specular geometry and (b) a nonpurely specular geometry where the angle between the LEO satellite velocity and the incident plane is 75° .

and the same Doppler range ($[-1000\ 1000]$ Hz). It is clear from Fig. 7(a) that in order to meet the 25×25 km spatial resolution requirement, the most suitable delay range is from -0.25 to 0.25 chips for the purely specular geometry, which coincides with the conclusion in [15]. The most suitable delay range is from -3 to 3 chips for the nonpurely specular geometry when the angle between the LEO satellite velocity and the incident plane is 75° .

D. Derivation of GMF

The DDMA versus wind direction, obtained from DDM simulated using the simulator for different wind speeds and incidence angles, is illustrated in Fig. 8. As observed, the DDMA is sensitive to wind direction, but it is also sensitive to wind speed and incidence angle. This indicates the dependence of DDMA on wind speed and incidence angle, which has been also observed in Sections III-B and V-B. Therefore, the GMF used in the wind direction retrieval algorithm is a function of multiple parameters (including wind direction, wind speed, and incidence angle). The GMF is derived empirically from the simulated training data formed as DDMA of different wind speeds and incidence angles.

From the plots in Fig. 8, it can be concluded that the behavior of the DDMA is the function of wind direction for different wind speeds and incidence angles. The form of the function is invariable, although the parameters of the function are related to wind speed and incidence angle. In order to find the best solution for the DDMA distribution, different simple fitting functions over wind direction have been tried. The expression used here to fit the DDMA distribution is

$$\text{DDMA} = a(U_{10}, \theta_i) + b(U_{10}, \theta_i) \cdot \cos(w\varphi_w) \quad (19)$$

where a , b , and w are the dependent coefficients of the fitting function, which are derived by minimizing the residuals between DDMA and wind direction; and a and b have different values for different wind speeds and incidence angles, which can be parameterized as a look-up-table (LUT). The DDMA curves and the best-fit curves are shown in Fig. 8.

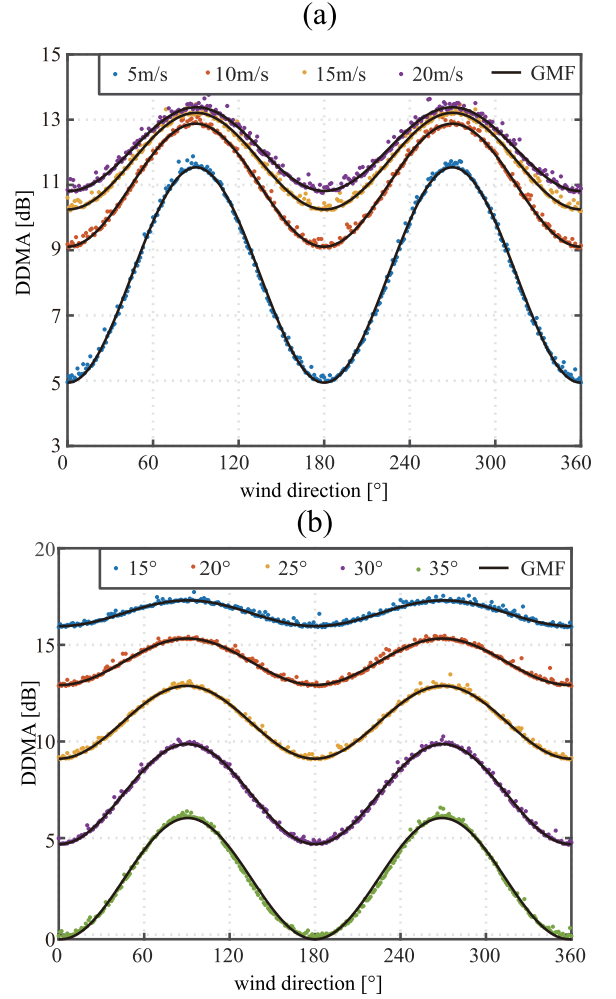


Fig. 8. Illustration of DDMA versus wind direction for (a) different wind speeds, the incidence angle of 25° , and (b) different incidence angles, the wind speed of 10 m/s. The scatter plots are the DDMA curves obtained from the DDM simulated using the simulator for different wind speeds and incidence angles. The black solid lines are the best-fit curves.

The total incidence angle range (from 15° to 35°) is divided into 201 intervals of 0.1° each, and the wind speed range (from 2 to 20 m/s) is divided into 37 intervals of 0.5 m/s each. The LUT of $a(U_{10}, \theta_i)$, $b(U_{10}, \theta_i)$, and w is derived for each interval by applying (19).

V. WIND DIRECTION RETRIEVAL ALGORITHM PERFORMANCE ANALYSIS

The performance of the proposed wind direction retrieval algorithm is assessed by using the test dataset simulated for different wind speeds and wind directions. The overall test dataset is finally composed of 1614 DDMs that we will use in the following performance studies.

A. Single-Satellite Observation

In the single-satellite observation, only the DDM from the one GNSS satellite is used to compute DDMA and retrieve wind direction. From the plots in Fig. 8, it can be concluded that the wind direction retrieved from a single-satellite DDM

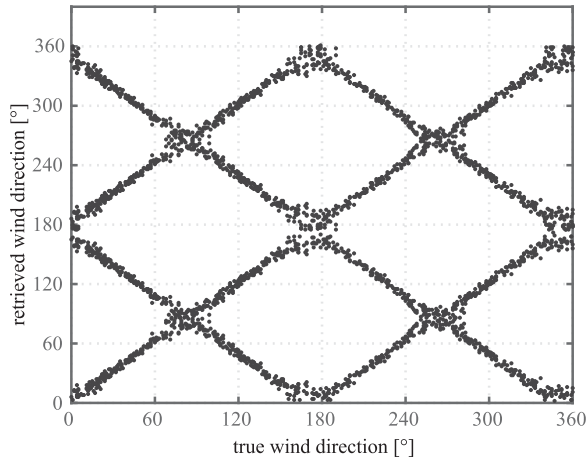


Fig. 9. Scatter plot of the true versus the retrieved wind direction using the GMF for the single-satellite observation.

presents four uncertain wind direction, since there are four wind directions corresponding to the same DDMA. The scatter plot of the true versus the retrieved wind direction is shown in Fig. 9. It is clear that the true wind direction (φ_w) corresponds to four possible solutions, including φ_w , $180^\circ - \varphi_w$, $180^\circ + \varphi_w$, and $360^\circ - \varphi_w$. This is due to the ambiguity of the observation geometry and the symmetry of the ocean spectrum. Multiple DDM measurements of the same ocean surface could be used to solve the observation geometry ambiguity.

B. Multisatellite Observation

The wind direction in this article is defined as the angle between the wind vector and the incident plane in the local coordinate systems defined in Section II-A. Therefore, different wind direction solutions will be obtained for the same wind direction relative to the north when the spaceborne GNSS-R receiver nadir antenna receives multiple scattered signals from the satellites of different azimuthal angles. And when the wind direction solutions retrieved from different azimuthal angles are converted to wind directions respect to North, the ambiguity of the measurement geometry will be eliminated. Therefore, in the multisatellite observation, the DDM from the GNSS satellites of different azimuthal angles is used to compute DDMA and retrieve wind direction. The scatter plot of the true versus the retrieved wind direction for the multisatellite observation is illustrated in Fig. 10. It can be seen that the true wind direction (φ_w) corresponds to two possible solutions, including φ_w and $180^\circ + \varphi_w$. The ambiguity of the measurement geometry has been eliminated. It is worth noting that the ambiguity cannot be eliminated if the difference in azimuthal angle of the satellites is a multiple of 90° .

C. Influence of Wind Speed

Wind speed has an important influence on the scattered signals in nonspecular geometry, which is the same as the purely specular scattering. The aforementioned analysis assumes that wind speed is retrieved accurately. However, it is difficult to

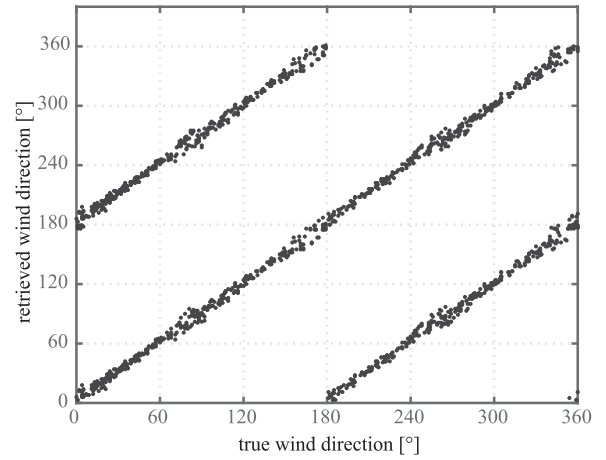


Fig. 10. Scatter plot of the true versus the retrieved wind direction using the GMF for the multisatellite observation.

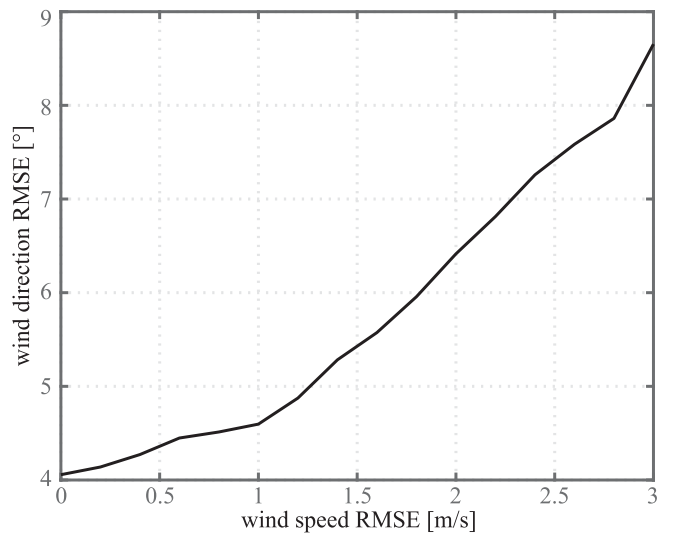


Fig. 11. Curve of the wind direction RMSE versus the wind speed RMSE, for the true wind speed of 15 m/s.

retrieve wind speed without any error using whether scattered GNSS signal in specular geometry or other measurement tools. The influence of wind speed error on the wind direction retrieval performance is evaluated using the test dataset from the simulator. The performance of the retrieval algorithm and wind speed error are characterized using rms error (RMSE). The RMSE is calculated as

$$\text{RMSE} = \sqrt{\frac{1}{N} \sum_{i=1}^N (\hat{\psi}_i - \psi_i)^2} \quad (20)$$

where the index i represents the different parameter samples; N is the number of the parameters samples; $\hat{\psi}_i$ and ψ_i are the i th the retrieved and true parameters, respectively, such as wind speed or wind direction. Wind direction RMSE curve as a function of the wind speed RMSE is shown in Fig. 11, which is calculated using simulated data in the true wind speed of 15 m/s. Compared with the wind direction obtained without taking into account of wind speed error, the worse measurement accuracy of

wind speed results in a larger RMSE of retrieved wind direction. Therefore, the accuracy of the wind speed needs to be improved to accurately retrieve the wind direction.

VI. CONCLUSION

Spaceborne GNSS-R has been significantly extended to a wide range of applications, especially the retrieval of ocean wind speed is gradually tending to be mature. These applications all use the GNSS-R purely in specular geometry. However, the scattered GNSS signal purely in specular geometry does not have enough sensitivity to wind direction, which then becomes difficult to retrieve. The wind direction can be retrieved using backward scattered GNSS signals. However, the power level of the backward scattered signal is too low to be received and processed, especially for spaceborne GNSS-R. Therefore, it is more likely to retrieve wind direction from spaceborne GNSS-R observables of the slightly nonspecular observation geometry between the purely specular and backward.

This article has theoretically investigated the influence of wind direction on spaceborne GNSS-R in the slightly nonspecular observation geometry. Simulation results show that the DDMA of spaceborne GNSS-R in nonspecular geometry can be used to retrieve wind direction. Therefore, the wind direction retrieval algorithm using DDMA of the nonspecular geometry is provided in this article. However, the DDMA is also affected by other parameters, such as wind speed and incidence angle, which makes it difficult to find a GMF with uniform parameters. And a LUT of GMF parameters is derived for different wind speeds and incidence angles. The wind direction retrieved in the single-satellite observation appears to have four variable uncertainty due to the double ambiguity. The ambiguity of the measurement geometry can be eliminated in the multisatellite observation, and two possible wind directions are presented in the wind direction retrieval algorithm.

Wind speed has an impact on the result of wind direction retrieval, therefore, it is important to improve the accuracy of wind speed. A high-gain LHCP antenna and high-sensitivity GNSS-R receiver should be used to receive and process the scattered GNSS signal in the nonspecular geometry because of its lower power level than the purely specular geometry. The 180° ambiguity could be eliminated by comparing the retrieved wind direction with available ground truth, such as *in situ* waves/wind direction data. Future improvements to the wind direction retrieval algorithm will focus on the development of hardware platform and calibration of the observable.

REFERENCES

- [1] M. Martín-Neira *et al.*, "A passive reflectometry and interferometry system (Paris): Application to ocean altimetry," *ESA J.*, vol. 17, no. 4, pp. 331–355, 1993.
- [2] W. Li, A. Rius, F. Fabra, E. Cardellach, S. Ribo, and M. Martín-Neira, "Revisiting the GNSS-R waveform statistics and its impact on altimetric retrievals," *IEEE Trans. Geosci. Remote Sens.*, vol. 56, no. 5, pp. 2854–2871, May 2018.
- [3] M. P. Clarizia, C. Ruf, P. Cipollini, and C. Zuffada, "First spaceborne observation of sea surface height using GPS-reflectometry," *Geophysical Res. Lett.*, vol. 43, no. 2, pp. 767–774, 2016.

- [4] W. Li, E. Cardellach, F. Fabra, S. Ribó, and A. Rius, "Lake level and surface topography measured with spaceborne GNSS-reflectometry from CYGNSS mission: Example for the lake Qinghai," *Geophysical Res. Lett.*, vol. 45, no. 24, pp. 13–332, 2018.
- [5] F. Wang, D. Yang, B. Zhang, W. Li, and J. Darrozes, "Wind speed retrieval using coastal ocean-scattered GNSS signals," *IEEE J. Sel. Topics Appl. Earth Observ. Remote Sens.*, vol. 9, no. 11, pp. 5272–5283, Nov. 2016.
- [6] A. Alonso-Arroyo, V. U. Zavorotny, and A. Camps, "Sea ice detection using UK TDS-1 GNSS-R data," *IEEE Trans. Geosci. Remote Sens.*, vol. 55, no. 9, pp. 4989–5001, Sep. 2017.
- [7] W. Li, E. Cardellach, F. Fabra, A. Rius, S. Ribó, and M. Martín-Neira, "First spaceborne phase altimetry over sea ice using TechDemoSat-1 GNSS-R signals," *Geophysical Res. Lett.*, vol. 44, no. 16, pp. 8369–8376, 2017.
- [8] A. Alonso-Arroyo, A. Camps, H. Park, D. Pascual, R. Onrubia, and F. Martín, "Retrieval of significant wave height and mean sea surface level using the GNSS-R interference pattern technique: Results from a three-month field campaign," *IEEE Trans. Geosci. Remote Sens.*, vol. 53, no. 6, pp. 3198–3209, Jun. 2015.
- [9] C. Chew, R. Shah, C. Zuffada, G. Hajj, D. Masters, and A. J. Mannucci, "Demonstrating soil moisture remote sensing with observations from the UK TechDemoSat-1 satellite mission," *Geophysical Res. Lett.*, vol. 43, no. 7, pp. 3317–3324, 2016.
- [10] A. Di Simone, H. Park, D. Riccio, and A. Camps, "Sea target detection using spaceborne GNSS-R delay-doppler maps: Theory and experimental proof of concept using TDS-1 data," *IEEE J. Sel. Topics Appl. Earth Observ. Remote Sens.*, vol. 10, no. 9, pp. 4237–4255, Sep. 2017.
- [11] W. Ji, C. Xiu, W. Li, and L. Wang, "Ocean surface target detection and positioning using the spaceborne GNSS-R delay-doppler maps," in *Proc. IEEE Geosci. Remote Sens. Symp.*, 2014, pp. 3806–3809.
- [12] S. Gleason *et al.*, "Detection and processing of bistatically reflected GPS signals from low earth orbit for the purpose of ocean remote sensing," *IEEE Trans. Geosci. Remote Sens.*, vol. 43, no. 6, pp. 1229–1241, Jun. 2005.
- [13] G. Foti *et al.*, "Spaceborne GNSS reflectometry for ocean winds: First results from the UK TechDemoSat-1 mission," *Geophysical Res. Lett.*, vol. 42, no. 13, pp. 5435–5441, 2015.
- [14] C. S. Ruf *et al.*, "The CYGNSS nanosatellite constellation hurricane mission," in *Proc. IEEE Int. Geosci. Remote Sens. Symp.*, 2012, pp. 214–216.
- [15] M. P. Clarizia and C. S. Ruf, "Wind speed retrieval algorithm for the cyclone global navigation satellite system (CYGNSS) mission," *IEEE Trans. Geosci. Remote Sens.*, vol. 54, no. 8, pp. 4419–4432, Aug. 2016.
- [16] C. S. Ruf, S. Gleason, and D. S. McKague, "Assessment of CYGNSS wind speed retrieval uncertainty," *IEEE J. Sel. Topics Appl. Earth Observ. Remote Sens.*, vol. 12, no. 1, pp. 87–97, Jan. 2019.
- [17] W. Li, E. Cardellach, F. Fabra, S. Ribó, and A. Rius, "Effects of PRN-dependent ACF deviations on GNSS-R wind speed retrieval," *IEEE Geosci. Remote Sens. Lett.*, vol. 16, no. 3, pp. 327–331, Mar. 2019.
- [18] J. L. Garrison, "Anisotropy in reflected GPS measurements of ocean winds," in *Proc. IEEE IGARSS Int. Geosci. Remote Sens. Symp. Proc.*, 2003, vol. 7, pp. 4480–4482.
- [19] C. Zuffada, T. Elfouhaily, and S. Lowe, "Sensitivity analysis of wind vector measurements from ocean reflected GPS signals," *Remote Sens. Environ.*, vol. 88, no. 3, pp. 341–350, 2003.
- [20] A. Komjathy, M. Armatys, D. Masters, P. Axelrad, V. Zavorotny, and S. Katzberg, "Retrieval of ocean surface wind speed and wind direction using reflected GPS signals," *J. Atmos. Ocean. Technol.*, vol. 21, no. 3, pp. 515–526, 2004.
- [21] E. Valencia, V. U. Zavorotny, D. M. Akos, and A. Camps, "Using DDM asymmetry metrics for wind direction retrieval from GPS ocean-scattered signals in airborne experiments," *IEEE Trans. Geosci. Remote Sens.*, vol. 52, no. 7, pp. 3924–3936, Jul. 2014.
- [22] S. Soisuvann, Z. Jelenak, F. Said, P. S. Chang, and A. Egido, "The GNSS reflectometry response to the ocean surface winds and waves," *IEEE J. Sel. Topics Appl. Earth Observ. Remote Sens.*, vol. 9, no. 10, pp. 4678–4699, Oct. 2016.
- [23] D. Guan *et al.*, "Wind direction signatures in GNSS-R observables from space," *Remote Sens.*, vol. 10, no. 2, 2018, Art. no. 198.
- [24] V. U. Zavorotny and A. G. Voronovich, "Recent progress on forward scattering modeling for GNSS reflectometry," in *Proc. IEEE Geosci. Remote Sens. Symp.*, 2014, pp. 3814–3817.
- [25] J. Park and J. T. Johnson, "A study of wind direction effects on sea surface specular scattering for GNSS-R applications," *IEEE J. Sel. Topics Appl. Earth Observ. Remote Sens.*, vol. 10, no. 11, pp. 4677–4685, Nov. 2017.
- [26] F. Wang, D. Yang, and L. Yang, "Feasibility of wind direction observation using low-altitude global navigation satellite system-reflectometry," *IEEE J. Sel. Topics Appl. Earth Observ. Remote Sens.*, vol. 11, no. 12, pp. 5063–5075, Dec. 2018.

- [27] V. U. Zavorotny and A. G. Voronovich, "Scattering of GPS signals from the ocean with wind remote sensing application," *IEEE Trans. Geosci. Remote Sens.*, vol. 38, no. 2, pp. 951–964, Mar. 2000.
- [28] A. G. Voronovich, *Wave Scattering From Rough Surfaces*. Berlin, Germany: Springer Science & Business Media, 2013, vol. 17.
- [29] T. Elfouhaily, B. Chapron, K. Katsaros, and D. Vandemark, "A unified directional spectrum for long and short wind-driven waves," *J. Geophysical Res., Oceans*, vol. 102, no. C7, pp. 15 781–15 796, 1997.
- [30] S. Gleason, C. S. Ruf, M. P. Clarizia, and A. J. O'Brien, "Calibration and unwrapping of the normalized scattering cross section for the cyclone global navigation satellite system," *IEEE Trans. Geosci. Remote Sens.*, vol. 54, no. 5, pp. 2495–2509, May 2016.
- [31] A. O'Brien, S. Gleason, J. Johnson, and C. Ruf, "The end-to-end simulator for the cyclone GNSS (CYGNSS) mission," *IEEE Trans. Geosci. Remote Sens.*, vol. 3, no. 2, pp. 306–315, 2014.
- [32] H. Park *et al.*, "A generic level 1 simulator for spaceborne GNSS-R missions and application to GEROS-ISS ocean reflectometry," *IEEE J. Sel. Topics Appl. Earth Observ. Remote Sens.*, vol. 10, no. 10, pp. 4645–4659, Oct. 2017.
- [33] J. W. Goodman, "Some fundamental properties of speckle," *JOSA*, vol. 66, no. 11, pp. 1145–1150, 1976.
- [34] S. Gleason, "Space-based GNSS scatterometry: Ocean wind sensing using an empirically calibrated model," *IEEE Trans. Geosci. Remote Sens.*, vol. 51, no. 9, pp. 4853–4863, Sep. 2013.
- [35] M. A. Richards, *Fundamentals of Radar Signal Processing*. New York, NY, USA: Tata McGraw-Hill Education, 2005.
- [36] D. K. Barton, *Radar System Analysis and Modeling*. Norwood, MA, USA: Artech House, 2004, vol. 1.
- [37] A. Alonso-Arroyo *et al.*, "SNR and standard deviation of CGNSS-R and IGNSS-R scatterometric measurements," *Sensors*, vol. 17, no. 1, 2017, Art. no. 183.
- [38] W. Li, E. Cardellach, F. Fabra, S. Ribó, and A. Rius, "Assessment of spaceborne GNSS-R ocean altimetry performance using CYGNSS mission raw data," *IEEE Trans. Geosci. Remote Sens.*, vol. 58, no. 1, pp. 238–250, Jan. 2020.



Guodong Zhang received the bachelor's degree in communication engineering from the School of Information Science and Engineering, Shandong University, Jinan, China, in 2015, the master's degree in communication and information engineering in 2017 from the School of Electronic and Information Engineering, Beihang University, Beijing, China, where he is currently working toward the Ph.D. degree in information and signal processing with Beihang University.

His current research interests include global navigation satellite system reflectometry application in ocean observation.



Dongkai Yang was born in 1972, in China. He received the B.S. degree in electronic engineering from the North University of China, Taiyuan, China, in 1994, and the M.S. and Ph.D. degrees in communication and information system from Beihang University, Beijing, China, in 1997 and 2000, respectively.

From 2001 to 2002, he was a Research Fellow with the Nanyang Technological University, Singapore. Since 2010, he has been a Full Professor with the School of Electronic and Information Engineering, Beihang University, Beijing, China. His current research interests include global navigation satellite system and its application.



Yongqing Yu was born in 1972, in China. He received the B.S. degree in weather forecast engineering from the China Petroleum & Chemical Corporation (SINOPEC) of China, Dongying, China, in 1995, and the Ph.D. degree in physical oceanography from the China Qingdao Institute of Marine Science Research Institute, Qingdao, China, in 2005.

His current research interests include ocean monitoring, weather forecasting and marine hazards warning.



Feng Wang received the bachelor's degree in electronic information engineering and the Ph.D. degree in communication and information engineering from the School of Electronic and Information Engineering, Beihang University, Beijing, China, in 2012 and 2018, respectively.

His current research interests include global navigation satellite system-reflectometry application in ocean observation.